Comparing gravity-based to seismic-derived lithosphere densities

A case study of the British Isles and surrounding areas

Root, Bart; Ebbing, J; van der Wal, Wouter; England, R.W.; Vermeersen, Bert

DOI
10.1093/gji/ggw483

Publication date
2017

Document Version
Final published version

Published in
Geophysical Journal International

Citation (APA)
Root, B., Ebbing, J., van der Wal, W., England, R. W., & Vermeersen, B. (2017). Comparing gravity-based to seismic-derived lithosphere densities: A case study of the British Isles and surrounding areas. *Geophysical Journal International*, *208*(3), 1796-1810. https://doi.org/10.1093/gji/ggw483

Geophysical Journal International

Geophys. J. Int. (2017) **208,** 1796–1810
Advance Access publication 2016 December 23
GJI Gravity, geodesy and tides

doi: 10.1093/gji/ggw483

Comparing gravity-based to seismic-derived lithosphere densities: a case study of the British Isles and surrounding areas

B.C. Root,[1] J. Ebbing,[2] W. van der Wal,[1] R.W. England[3] and L.L.A. Vermeersen[1]

[1]*Astrodynamics & Space Missions, Delft University of Technology, Kluyverweg* 1, 2629 *HS Delft, The Netherlands. E-mail: b.c.root@tudelft.nl*
[2]*Department of Geophysics, Christian-Albrechts-Universität, D-*24118 *Kiel, Germany*
[3]*Department of Geology, University of Leicester, Leicester LE*1 7*RH, United Kingdom*

Accepted 2016 December 21. Received 2016 December 19; in original form 2016 June 13

SUMMARY

Lithospheric density structure can be constructed from seismic tomography, gravity modelling, or using both data sets. The different approaches have their own uncertainties and limitations. This study aims to characterize and quantify some of the uncertainties in gravity modelling of lithosphere densities. To evaluate the gravity modelling we compare gravity-based and seismic velocity-based approaches to estimating lithosphere densities. In this study, we use a crustal model together with lithospheric isostasy and gravity field observations to estimate lithosphere densities. To quantify the effect of uncertainty in the crustal model, three models are implemented in this study: CRUST1.0, EuCrust-07 and a high-resolution *P*-wave velocity model of the British Isles and surrounding areas. Different *P*-wave velocity-to-density conversions are used to study the uncertainty in these conversion methods. The crustal density models are forward modelled into gravity field quantities using a method that is able to produce spherical harmonic coefficients. Deep mantle signal is assumed to be removed by removing spherical harmonic coefficients of degree 0–10 in the observed gravity field. The uncertainty in the resulting lithosphere densities due to the different crustal models is ± 110 kg m^{-3}, which is the largest uncertainty in gravity modelling. Other sources of uncertainty, such as the V_P to density conversion (± 10 kg m^{-3}), long-wavelength truncation (± 5 kg m^{-3}), choice of reference model ($< \pm 20$ kg m^{-3}) and Lithosphere Asthenosphere Boundary uncertainty (± 30 kg m^{-3}), proved to be of lesser importance. The resulting lithosphere density solutions are compared to density models based on a shear wave velocity model. The comparison shows that the gravity-based models have an increased lateral resolution compared to the tomographic solutions. However, the density anomalies of the gravity-based models are three times higher. This is mainly due to the high resolution in the gravity field. To account for this, the gravity-based density models are filtered with a spatial Gaussian filter with 200 km half-width, which results in similar density estimates (± 35 kg m^{-3}) with the tomographic approach. Lastly, the gravity-based density is used to estimate laterally varying conversion factors, which correlate with major tectonic regions. The independent gravity-based solutions could help in identifying different compositional domains in the lithosphere, when compared to the tomographic solutions.

Key words: Gravity anomalies and Earth structure; Mantle processes; Europe.

1 INTRODUCTION

There is abundant evidence that the lithosphere is highly heterogeneous (Jordan 1975; Afonso *et al.* 2008; Griffin *et al.* 2009; Kaban *et al.* 2016). Variations in temperature and composition at lithospheric depths result in laterally varying shear wave velocity and density anomalies (Khan *et al.* 2015). Thus, temperature and composition can be studied by using seismic observations (Afonso *et al.* 2016a) and gravity modelling (Kaban *et al.* 2004; Herceg *et al.* 2016) or in joint-inversion studies combining both techniques (Forte *et al.* 1994; Deschamps *et al.* 2001; Simmons *et al.* 2010; Cammarano *et al.* 2011; Khan *et al.* 2015). However, all these studies have their limitations, which result in uncertainties in the final model of the lithosphere (Foulger *et al.* 2013).

Several V_S models are available for the upper mantle (e.g. Ritsema *et al.* 2011; Schivardi & Morelli 2011; Debayle & Ricard 2012; Schaeffer & Lebedev 2013). The velocity anomalies are caused by temperature, density, and composition changes in the

upper mantle (Jordan 1978) and point to a complex structure in the lithosphere. There are other causes as well, for example, anisotropy due to crystal structure or pre-stress anisotropy, but the effect of temperature is believed to be the most important (Forte 2007). One of the drawbacks of passive seismic experiments, such as delay time analysis, receiver functions and traveltime tomography, is the uneven distribution of the seismic events and receiver stations. Areas without any data or sparse data coverage need interpolation and result in large uncertainties. A second drawback is that some of these techniques need an *a priori* crustal model to account for the corresponding traveltime corrections (Schaeffer & Lebedev 2013). Unmodelled crustal effects introduce errors in the lithosphere region (Lekić & Romanowicz 2011; Schaeffer & Lebedev 2013). Furthermore, the 3-D structure of the wave-speed anomalies is difficult to determine because of the smearing problem along the ray bundles (Foulger *et al.* 2013). Moreover, the wave velocities are not uniquely related to parameters like temperature, or composition. The wave velocities are related to elastic parameters (Artemieva 2001), which are influenced by temperature and composition. The relations between elastic parameters, temperature, and composition are determined in the laboratory and have their own uncertainties (Cammarano *et al.* 2011). Finally, shear wave observations are found to be insensitive to density variations (Khan *et al.* 2015). A detailed review of tomographic imaging is given in Foulger *et al.* (2013), the uncertainty in the V_S models proves to be difficult to quantify.

Lithospheric structures can also be explored by using the gravity field (e.g. Kaban *et al.* 2004; Root *et al.* 2015; Herceg *et al.* 2016). However, due to the intrinsic non-uniqueness of gravity modelling the solutions need to be constrained, which introduces uncertainties in the final model. First, the long wavelength features in the gravity field are assumed to be from the deep mantle (below 300 km) or even core-mantle boundary effects (Forte *et al.* 1993). Usually, these features are removed by removing low-degree spherical harmonic coefficients from the gravity field observations. For example, the regional study of Herceg *et al.* (2016) used a truncation limit of degree and order 10 in agreement with Bowin (1991, 2000). This particular truncation corresponds to removing signals with wavelengths larger than 2000 km. Second, the gravity signal of the crust needs to be removed from the observations (Kaban *et al.* 2004) to reveal the lithosphere. Errors in the used crustal model lead to uncertainty in the lithosphere solutions (Panasyuk & Hager 2000; Kaban *et al.* 2004; Root *et al.* 2015). For example, the global crustal model CRUST1.0 (Laske *et al.* 2013) suffers from lack of data in large parts of the world.

Regional crustal structures can also be observed by high-resolution seismic observations, like wide-angle seismic data in the form of *P*-wave velocity (V_P) models, and can be converted to density profiles (e.g. Kelly *et al.* 2007; Tesauro 2008; Artemieva & Thybo 2013). A high-resolution V_P model of the British isles and surrounding areas was presented by Kelly *et al.* (2007), together with uncertainty estimates of the seismic observations. This regional V_P model is used in the present study to study the effect of increased radial resolution in crustal models. The high-resolution observations in these models reduce the uncertainty in crustal structure compared to global models and should therefore result in improved lithosphere models.

Finally, many joint studies using seismic models and gravity observations have been performed. After a joint study of seismic wave velocities and gravity observation, Forte *et al.* (1994) found that the mantle heterogeneities from seismic observations fit the long wavelengths of the potential field, but have a large mismatch to the free-air anomalies. Others estimated the scaling factor between shear wave and density (Deschamps *et al.* 2001). They also found that the geoid between spherical harmonics coefficients 11–16 is most sensitive to lithosphere anomalies. More sophisticated models have been developed, where seismic wave observations were combined with gravity data, plate motions, dynamic topography and mineral physics such as the GYPSUM model (Simmons *et al.* 2010). Cammarano *et al.* (2011) found that by inserting a petrological lithosphere, the fit to geoid and topography data improved. Moreover, they introduced lateral compositional variations in the lithosphere did not change the thermal interpretation of the seismic models significantly, which shows that the seismic waves have different sensitivities to the fundamental parameters of temperature and composition. Another study proposed to include electrical conductivity in the joint lithosphere studies, due to its different sensitivity to temperature and composition (Khan *et al.* 2015). The most advanced joint inversion studies are characterizing the thermochemical structure of the lithosphere using seismic data, gravity observations, and surface heat flow, together with geochemical information of the rock composition (Afonso *et al.* 2013a,b, 2016b).

In this study, we focus on the exploration of lithospheric density structures using mainly the gravity field to fully understand the possibilities and limitations of this observation. We examine the uncertainty of the gravity-based density modelling of the lithosphere. In order to do this, we propose a new gravity modelling approach to estimate lithosphere densities. This methodology makes use of a crustal model, lithosphere isostasy, and gravity field observations. Constraints needed in the modelling such as the crustal model, truncation of the gravity data, and Lithosphere Asthenosphere Boundary (LAB) model introduce uncertainties in the final lithosphere densities. We will quantify these uncertainties for the different constraints. After this, the question arises of how a gravity-based lithosphere compares to a seismic-derived lithosphere? The seismic tomography models have their own uncertainties and drawbacks. Especially, the sensitivity of V_S tomography to density is limited. Nevertheless, the comparison between the two approaches is useful as a first step to see if a meaningful lithospheric density model can be derived from a purely gravity based model

In the first section, uncertainties due to the crustal model will be quantified. The crustal models use different V_P observations, different V_P to density conversion relations, and different radial resolution. Section 2 discusses the different crustal models that are used in this study. Second, the effect of the long wavelength truncation of the gravity field and its effect on the estimation of the lithospheric densities is examined. Moreover, we look at the uncertainties introduced by selecting a LAB model and an isostatic reference model. Section 5 shows the resulting lithospheric densities of the different models and their fit to the gravity fields. Finally, we discuss the differences between gravity-based and tomography-based lithosphere densities.

2 CRUST MODELS

The region of the British Isles and surrounding areas is well covered by seismic profiles and contains oceanic crust, continental margin, elevated continental crust, and cratonic crust. This makes it a good region to explore differences in gravity-based lithosphere densities due to crustal model uncertainties and evaluate the proposed methodology for different tectonic regions. The impact on the final lithosphere model of the different crustal models is examined. Also uncertainties due to the V_P to density conversion discussed in Section 2.2 are studied.

To investigate the error introduced by the uncertainty in crustal models, three crustal models are used in this study. Model A is the global representation of the crust by CRUST1.0 (Laske *et al.* 2013). The seismic observations are converted to density by using conversions for sedimentary rock (Gardner *et al.* 1974) and the Christensen & Mooney (1995) conversions (CM95) for depth-dependent crustal rock. Model B will use the regional crustal model EuCrust-07 (Tesauro 2008), which consists of one sedimentary layer and two crystalline-crust layers. The model covers the area between 35°N–71°N, 25°W–35°E. Model C is constructed from a regional V_P model of the British Isles and surrounding areas (Kelly *et al.* 2007). The implementation of this model is discussed in Section 2.1. It has a high-resolution representation of the crustal masses, especially in the radial direction, compared to Models A and B. Model B has used similar data for the area as Model C. This makes it possible to study the effect of increased radial resolution in a crustal model. For both regional models, the crustal masses outside the study area are complemented by the CRUST1.0 model (Laske *et al.* 2013) and interpolated on a 0.5 × 0.5 arc-deg grid.

2.1 Regional V_P model (Model C)

The regional V_P model that is used to compare with CRUST1.0 in this study is an updated version of Kelly *et al.* (2007). The updates consist of the LISPB-Delta data, which runs NNW–SSE across Wales and SW England and fills an important gap in observations of the crustal structure (Maguire *et al.* 2011). Furthermore, new data is added in southern Scandinavia from the MAGNUS REX profiles (Stratford *et al.* 2009; DeGiorgio 2012). The model describes the crustal seismic velocity structure of the British Isles and surrounding areas and uncertainty in the velocity model (Fig. 1). The seismic observations suffer from coupled uncertainties between velocity and depth of the interfaces (Kelly *et al.* 2007) that makes it difficult to determine if the uncertainty is in the velocity distribution or the geometric boundaries. Nevertheless, it is constructed using 3-D Kriging designed from an analysis of variograms derived from the seismic data (for details see Kelly *et al.* 2007). The advantage of this interpolation is that there is an error estimate of the *P*-wave velocity solution. The maximum depth of the model extends to around 60 km underneath the Fennoscandian craton. The radial density resolution is an improvement compared to the eight-layered CRUST1.0 crustal model and the three-layered EuCrust-07 model.

A cross-section of the model (Fig. 2) shows the radial distribution of the *P*-wave velocity anomalies and their uncertainties. Sedimentary bodies are defined by velocities ranging between 2.27 and 5.0 km s^{-1}. Crustal velocities, close to the crust-mantle boundary, can go up to approximately 7.8 km s^{-1}. The uncertainty of the V_P model is more visible in the uncertainty map in Fig. 1, where the locations of seismic profiles are easily identified. Locations with seismic observations have an uncertainty of ±0.5–0.8 km s^{-1}, whereas areas without observations have uncertainties of more than ±1.8 km s^{-1} around the mean velocity. Fig. 2(b) shows no clear increase or decrease of uncertainty with increasing depth.

The topography is obtained from ETOPO1 (Amante & Eakins 2009). The Moho boundary is defined as the transition between crustal and upper mantle material at $V_P = 7.8$ km s^{-1}. The Moho is very deep in Fennoscandia (Kinck *et al.* 1993; Korsman *et al.* 1999) and becomes gradually shallower to the southwest. Away from the continental plateau the Moho is found to be at depths shallower than 20 km, where oceanic lithosphere can be found. In the Fennoscandian area all sedimentary material has been removed by recent glacial periods (Steffen & Wu 2011). Also, Iceland is free of sediments, because it is relatively new land due to the diverging plate boundary. A number of prominent sedimentary basins are present in the study area (see Fig. 1): the Porcupine Basin, the Biscay margin, the Rockall Through and the Mid-Norwegian Basin. These basins have depths to the basement of up to 10–12 km. In the

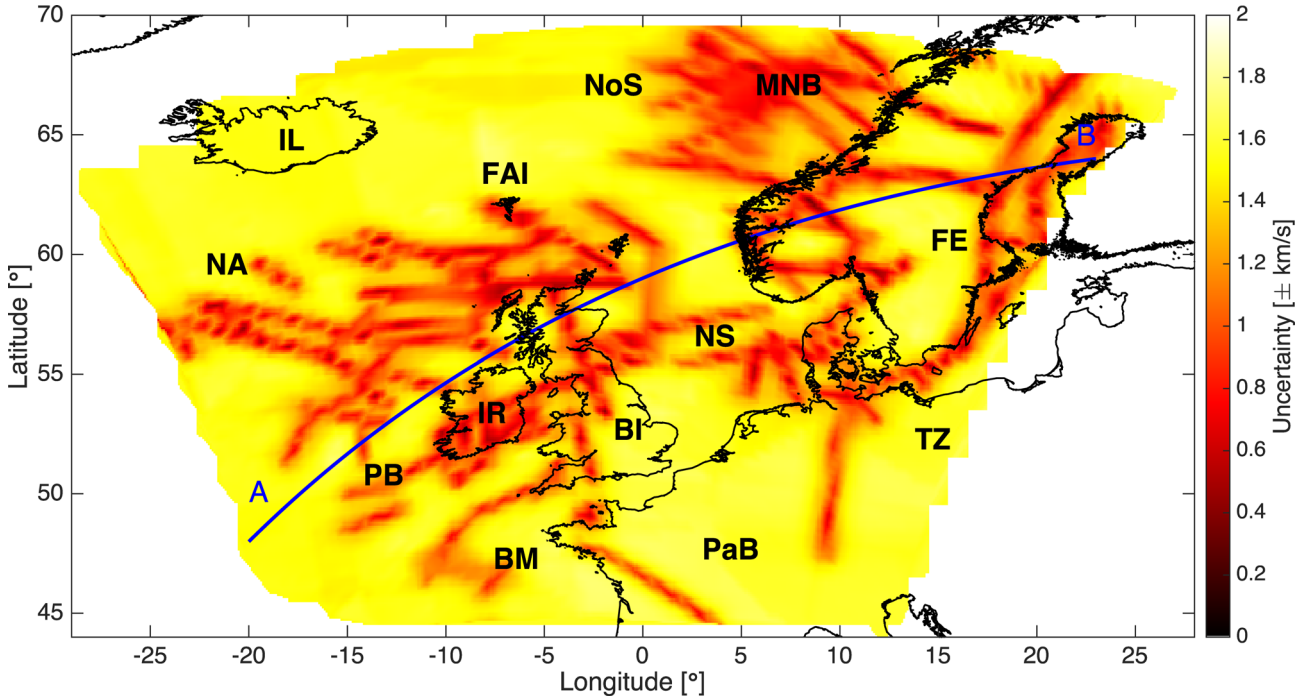

Figure 1. Depth-average of the uncertainty in the *P*-wave velocity model. The blue line denotes a cross section AB that is shown in Fig. 2. Several locations that are used: BI, British Isles; BM, Biscay Margin; FE, Fennoscandian craton; FAI, Faroe Islands; IL, Iceland; IR, Ireland; MNB, Mid-Norwegian Basin; NA, North Atlantic ocean; NoS, Norwegian Sea; NS, North Sea; PaB, Paris Basin; PB, Porcupine Basin; TZ, Tornquist Zone.

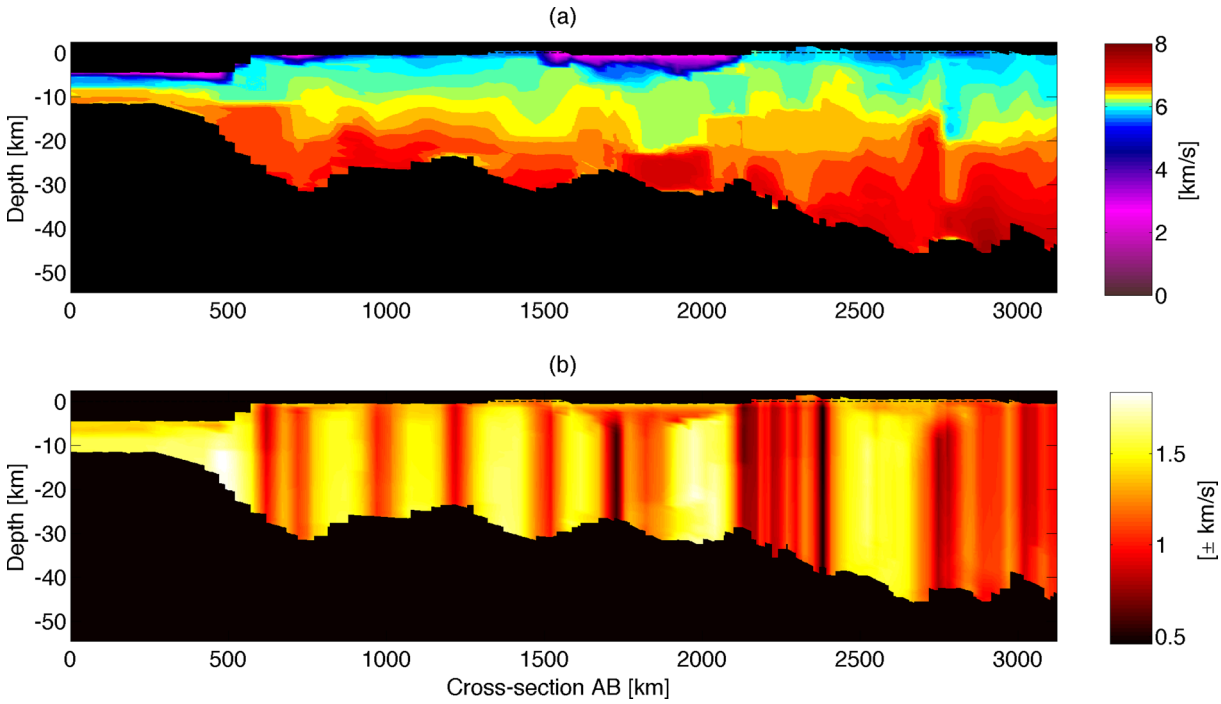

Figure 2. Cross-section AB (see Fig. 1) through the regional V_P crustal model (Kelly *et al.* 2007) with (a) the V_P values and (b) the uncertainty of the *P*-wave velocity.

Mid-Norwegian Basin area an improved structure of the sedimentary basins is expected, because many more seismic profiles were available in the regional model compared to CRUST1.0. The large-scale, but shallow, sedimentary basin northeast of Faroe Islands is not present in the sediment layer. This can be related to an absence of constraining data in the model in that region.

2.2 Transformation to density model

Averaged relations between crustal *P*-wave velocities and density are usually empirically determined (Brocher 2005). We use two common relations to study the effect of the conversion uncertainty on the density modelling of the crust: the Nafe–Drake relation (Ludwig *et al.* 1970) and the Gardner/CM95 relations (Christensen & Mooney 1995). Fig. 3 illustrates the two different relations between *P*-wave velocities and density. These relations are used in many modelling studies (Kaban *et al.* 2014; Tesauro *et al.* 2014; Herceg *et al.* 2016).

First, the Nafe–Drake relation relates V_P observations to density for sedimentary and crustal rocks. A review of the Nafe–Drake relation is made by Brocher (2005), who reviewed the data and estimated a simple relation through all the data. Second, the Gardner/CM95 conversion uses the Gardner rule (Gardner *et al.* 1974) for sedimentary rocks and the empirically determined relations of Christensen & Mooney (1995) for the crystalline-crustal rocks. Zoback & Mooney (2003) found a small error in Christensen & Mooney (1995). The (Christensen & Mooney 1995) relations have different depth dependencies for crustal rocks, which is illustrated by the different lines in Fig. 3. The two conversions have an overall similar shape. The main difference between the two relations is that the Nafe–Drake relationship produces a crust that has an overall lower density than the Gardner/Christensen–Mooney relation. This means that the crustal signal plays a slightly smaller role in the overall gravity signal of the complete lithosphere signal.

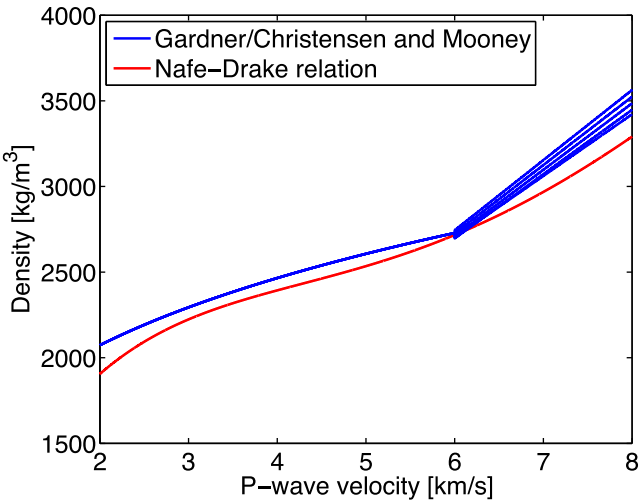

Figure 3. The relation between crustal density and *P*-wave velocity according to two studies. The red line shows the Nafe–Drake relationship (Ludwig *et al.* 1970) and the blue line shows the Gardner rule for sedimentary rocks, complemented by empirical relations of Christensen & Mooney (1995) for crustal rocks, which are depth dependent.

3 LITHOSPHERE MODELS

Here, we present a procedure to estimate the density distribution in the lithospheric part of the upper mantle by using gravity observations and a density model of the crust. First, lithospheric densities are computed by assuming isostatic equilibrium. This isostatic model is then used as a starting model for fitting lithosphere densities to the gravity field. This will produce the values for the lateral densities in the lithosphere. Finally, we describe the procedure to obtain density anomalies from *S*-wave tomography models, such that they can be compared to the gravity-based solution. For a thorough discussion

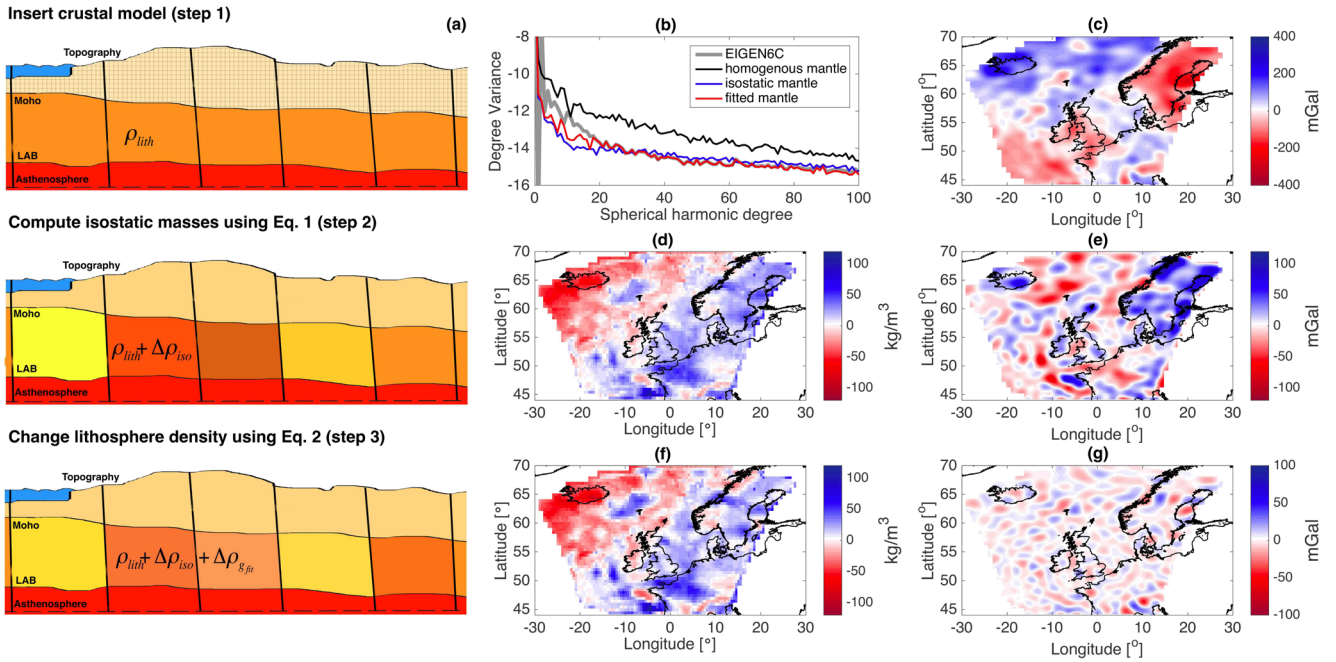

Figure 4. (a) A sketch of how the gravity-based lithosphere model is constructed in three steps: first a crustal model is selected and complemented by a lithosphere and asthenosphere up to 300 km depth. Then lithospheric density anomalies are computed using lithosphere isostasy with equal pressure at 300 km (eq. 1). Finally, the lithospheric densities are changed such that the complete model is fitted to the gravity field. (b) the degree variance of the gravity fields of the observations and density models during the three steps. (d,f) The density maps of the lithosphere after step 2 and 3, respectively. (c) Gravity residual of EIGEN6C with the model at step 1. (e) Gravity residual of EIGEN6C with the model at step 2 (isostatic model). (c) Gravity residual of EIGEN6C with the model at step 3 (fitted model).

on the uncertainties in *S*-wave tomography we refer to Foulger *et al.* (2013) or Afonso *et al.* (2016a).

3.1 Gravity-based model of the lithosphere

In order to construct a lithosphere model both gravity field observations and the concept of isostasy are used. The construction of the lithosphere model is done in three steps (Fig. 4a). First, a crustal model is chosen which is complemented by a reference mantle density (ρ_m) up to 300 km depth. The different crustal models are discussed in Section 2. Second, an *a priori* model of the lithosphere density anomalies ($\Delta\rho_{\mathrm{iso}}$), assuming lithospheric isostasy (Turcotte & Schubert 2014), is computed (see Fig. 4d). In the third step, the model is completed by computing extra lateral density anomalies ($\Delta\rho_{g_{\mathrm{fit}}}$) in the lithosphere (Fig. 4f) needed to reduce the gravity residual of the model in line with the observed gravity. Fig. 4(b) shows the improvement of the gravity field fit of the models to observations. With a homogeneous lithosphere, the degree variance of the gravity results is one order larger than the observed gravity field, which results in residual gravity anomalies of $\pm$400 mGal (Fig. 4c). When lithospheric isostasy is used the degree variance drops to the same order as the observed field, reducing the residuals to $\pm$100 mGal (Fig. 4d). Step 3 reduces the residuals to $\pm$45 mGal, removing any correlation in the residual with geological structures (Fig. 4g).

Crustal masses are assumed to be compensated in the upper mantle, which we define from now on as the lithosphere. These variations in the density structure are stable over a long timescale, because the lithosphere is not involved in mantle convection (Jordan 1975). The lower boundary of this region is referred to as the LAB. The temperature at that boundary is estimated to be between 1250 and 1350 °C, which represents the boundary between a conducting and convecting thermal regime (Artemieva 2001, pp. 7). This corroborates our assumption that compensated masses are situated in the region between the LAB and the Moho. The compensation is shown to represent the global gravity observations well in most of the spectral domain (Root *et al.* 2015). The separation between the lithosphere and asthenosphere is obtained from Hamza & Vieira (2012), which is based on global databases of heat flow (Vieira & Hamza 2010) and crustal structure (Laske *et al.* 2013). We deliberately choose not to use an LAB obtained from seismic tomography data to be independent from that data set.

To establish isostatic equilibrium, each mass column in the density model will be equal to the mass of a column of the reference model. The reference mass ($\rho_{\mathrm{ref}}V_{\mathrm{lith}}$) column consists of a 30 km thick crust with a density of 2850 kg m^{-3} complemented by a mantle with a density of 3300 kg m^{-3}. These crustal thickness and density values are chosen after inspection of the CRUST1.0 model. The average crustal thickness and density in areas were the model has 0 ± 50 m topography are estimated to be around these values. The sensitivity of these chosen values and their effect on the final result will be presented in Section 5. The following relation for every mass column (i) can be set up:

$$\int_{300\,\mathrm{km}}^{0\,\mathrm{km}} \rho_{\mathrm{ref}}\,\mathrm{d}V = \int_{\mathrm{Moho}}^{\mathrm{topo}} \rho_{\mathrm{crust},i}\,\mathrm{d}V + \int_{\mathrm{LAB}}^{\mathrm{Moho}} \rho_{\mathrm{lith}}\,\mathrm{d}V + \int_{300\,\mathrm{km}}^{\mathrm{LAB}} \rho_{\mathrm{asth}}\,\mathrm{d}V + \int_{\mathrm{LAB}}^{\mathrm{Moho}} \Delta\rho_i\,\mathrm{d}V \qquad (1)$$

The mass of the crust will be determined by computing the spherical volume and multiplying it with the density from the converted *P*-wave velocity model or CRUST1.0. The mantle part of the model is constructed from the initial lithosphere (ρ_{lith}) with a density of 3330 kg m^{-3} and is complemented by an asthenosphere up to 300 km

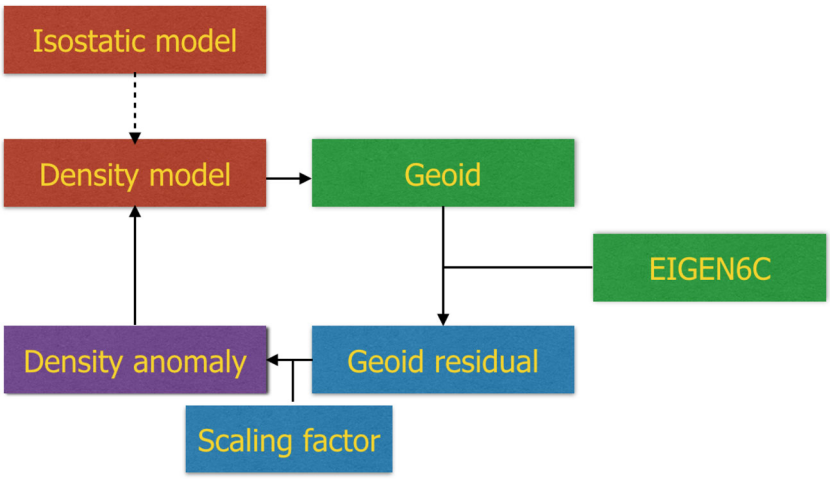

Figure 5. The iteration process starts with the *a priori* isostatic model. Gravity field quantities of the density model are computed using the spectral forward modelling method described in Root *et al.* (2016). The geoid is compared with the EIGEN6C gravity model and a residual field is calculated. This residual is normalized and scaled to construct a density map that is added to the lithosphere density of the model to improve the fit to the gravity field. This process is repeated until convergence is obtained.

deep using a homogeneous density of 3300 kg m^{-3}. The extra mass ($\Delta\rho_i$) needed to compensate the crust is calculated between the Moho and LAB, and added to the initial lithosphere density.

The isostatic model can be improved to better fit the observed gravity field. In step 3 of the gravity modelling, the lithosphere density is changed such that the complete density model better fits the gravity observations. Fig. 5 illustrates the iterative process in a flow chart. It starts by computing the gravity field solution of the isostatic density model. This solution is compared with gravity model EIGEN6C (Shako *et al.* 2014). It was found that the geoid (N) has the best convergence properties in this process, and that it is sensitive to lithospheric structures. The normalized geoid residual is used to calculate a density anomaly:

$$\Delta\rho_i = \sigma \frac{N_{\mathrm{EIGEN6C}} - N_{\mathrm{model},i}}{|(N_{\mathrm{EIGEN6C}} - N_{\mathrm{model},i})|_{\max}}. \quad (2)$$

This density anomaly, $\Delta\rho_i$, is added to the lithospheric density of the old model, to be used in the next iterative step (n). The scaling parameter, σ, ensures that the process converges within respectable time. This is repeated several times until the geoid residual between the modelled and observed field converges. Fig. 4(h) shows the final results of the fitting process. Almost all of the density changes due to the gravity fitting process are smaller than ± 25 kg m^{-3} compared to the isostatic lithosphere model (step 2). This shows that lithospheric isostasy is a good first order approximation for the density distribution in the lithosphere.

3.2 Tomographic model of the lithosphere

In this study, the seismological density model of the lithosphere is based on SL2013sv (Schaeffer & Lebedev 2013). To obtain the density of the lithosphere, the conversion factor from (Karato 2008, p. 373) is used to convert the lithospheric S-wave velocities to density values which can be compared to the gravity-based lithosphere structures of this study. The conversion factor is defined by the following relation:

$$\frac{\Delta\rho}{\rho} = p\frac{\Delta V_S}{V_S}. \quad (3)$$

A constant conversion factor (p), or scaling factor, of around 0.2 is suitable for the lithospheric region (Karato 2008, p. 377), this value is also approximately used by other models (Steinberger 2016). We assume that all S-wave anomalies are caused by thermal effects. The purpose of this study is not to determine the best estimates of mantle temperatures from seismic observations, but to study the differences between the two approaches.

With the estimated densities from gravity observations, we are able to determine a conversion factor (Forte & Mitrovica 2001) that varies in lateral but not in radial direction. We compare these lateral variations in the conversion factor with tectonic settings of the area. Because the estimated density is an average density anomaly for the lithosphere, the V_S anomalies must be radially averaged before they are converted to density. Here, the lithosphere is defined by the same area between the Moho and the LAB used in the gravity modelling, ensuring that the same regions are compared. Introducing radially varying density estimates in the lithosphere is for future studies. The conversion factor can be used to see the influence of temperature and composition on the shear wave velocity distribution of the lithosphere. A positive conversion factor usually means a temperature anomaly, whereas a negative value could indicate compositional effects (Cammarano *et al.* 2003), but in many cases the anomaly has contributions from both. The ratio can readily become infinity, if one of the two fields is small. Therefore, we neglect locations where $\frac{\Delta\rho}{\rho} < 0.05$ per cent and $\frac{\Delta V_S}{V_S} < 0.02$ per cent.

4 FORWARD GRAVITY MODELLING

The density models are converted into a gravitational potential field using a spherical harmonic forward modelling technique (Rummel *et al.* 1988; Novák & Grafarend 2006; Root *et al.* 2016). This method divides the density model in several spherical density layers that can have both lateral density variations and varying upper and lower boundary layers. The separate layers are converted to spherical harmonic coefficients representing the gravity potential field of that layer. This is done with a global spherical harmonic analysis using a weighted least squares algorithm (Sneeuw 1994), that estimates the spherical harmonic coefficients (V_{nm}) from the density and geometry

of the layer. The potential field (V) of the layer is represented as follows:

$$V(r, \Omega) = \frac{GM}{R} \sum_{n,m}^{\infty} \left(\frac{R}{r}\right)^{n+1} V_{nm}\, Y_{nm}(\Omega), \quad (4)$$

where Y_{nm} represents the fully normalized associated Legendre functions and Ω is a shorthand notation for the lateral coordinates longitude and latitude. Multiple layers are analysed and combined, which results in a gravity potential solution for the complete density structure.

To ensure high resolution in the radial structure the forward model consists of several layers starting with a radial thickness of 2.5 km, starting with the topography up to 10 km depth. From 10 km depth up to the Moho, the layers will have an increased thickness of 5 km. The lithosphere and asthenosphere layers will have a thickness of 25 km. This thin layering is needed to satisfy the convergence criterion of the spectral forward method (Root *et al.* 2016) and preserve the high-resolution information of Model C.

5 RESULTS

To quantify the effect of the different constraints in our modelling, we show the results of the various lithosphere models due to varying crustal models, V_P-to-density conversions, long-wavelength truncation of the gravity data, choice of reference model, and LAB. The difference between crustal models A and B gives information about the uncertainty in crustal models, whereas the difference between Models B and C gives information about the effect of increased radial resolution in the crustal model. In all three cases, our modelled lithosphere densities are in the range of ± 110 kg m^{-3}. After the model comparisons, the uncertainty due to spherical harmonic truncation, isostatic reference model, and uncertainty in LAB model is considered.

Table 1 states the statistics of the differences of observed and modelled gravity field quantities both for the geoid and for the gravity anomaly. All values, mean (μ) and standard deviation (σ), should be zero for a perfect fit to the observations. So, these statistics are parameters to judge the performance of the modelled gravity solution to the observed gravity field. Model B has the highest standard deviation (12.2 and 11.9 mGal) from the gravity observations. The other models show a small improvement (Model A is 8.04, and Model C are 9.43 and 8.06 mGal). Similar observations can be gathered from the geoid misfit results and it can be seen that the iterative gravity fitting converges to a geoid anomaly standard deviation ranges from 0.45 to 0.65 m.

Furthermore, the gravity field residuals maps in Figs 6(a)–(c) show gravity field variations of approximately ± 45 mGal in mostly random-looking patterns. Similar to in the table results, Model B has a higher residual compared to the other two models. In Model C a boundary misalignment at the eastern border of the study area is visible. The cratonic crust in CRUST1.0 compared to the regional model produces a large step in the mass of overall density model, resulting in an erroneous gravity anomaly. The rest of the study area shows no large residuals in the three model solutions. Overall, there is little correlation between the gravity residuals and geologic structures, which also suggests a proper model fitting to the gravity field for the different lithosphere models.

5.1 Crustal models

The bottom part of Table 1 shows the statistics of the lithosphere density solutions. The lithosphere densities have a variation of ± 110 kg m^{-3} around their mean value. These values are within reasonable mantle density estimates, when compared to other estimates for variation in mantle density, for example, ± 150 kg m^{-3} (Kaban *et al.* 2004). The mean mantle density in the different models is between 3300 and 3328 kg m^{-3}. An interesting observation is that the mean value of Model A (CRUST1.0) is similar to the Nafe–Drake models instead of the CM95 conversion relations.

Figs 6(d)–(f) show the column-averaged density anomalies of the lithosphere with respect to the reference density of 3330 kg m^{-3}. The density anomaly maps from the three models illustrate the uncertainty introduced by the crustal models. Density anomalies become more positive when travelling from the oceanic to the continental lithosphere part of the region. In all three models, the lowest lithospheric density is found underneath Iceland. This can be explained by the existence of the spreading ridge, where hot asthenosphere is brought to the surface. The high temperature decreases the density of the mantle material with respect to the continental lithosphere. Higher density is found underneath the continental crust to compensate the buoyant continental crust (Christensen & Mooney 1995). The most visible difference between Model A and Models B and C is the density estimate of the lithosphere underneath Fennoscandia, which can be linked to the Baltic craton. Model A shows a

Table 1. Top part of the table shows statistical values of differences between forward modelled gravity field and gravity observation of EIGEN6C. The bottom part shows the statistics of the estimated lithospheric density anomalies. μ and σ are mean and standard deviation, respectively.

	Geoid		Gravity	
	μ (m)	σ (m)	μ (mGal)	σ (mGal)
EIGEN6C - Model A	− 0.04	0.43	− 0.05	8.04
EIGEN6C - Model B: CM95	− 0.0024	0.66	0.08	12.2
EIGEN6C - Model B: NafeDrake	− 0.0006	0.65	0.06	11.9
EIGEN6C - Model C: CM95	− 0.08	0.51	− 0.72	9.43
EIGEN6C - Model C: NafeDrake	− 0.06	0.44	− 0.39	8.06
	Density			
Model	μ (kg m^{-3})	σ (kg m^{-3})	min (kg m^{-3})	max (kg m^{-3})
Model A	− 15.8	32.2	− 121.5	104.8
Model B: CM95	− 20.5	28.0	− 112.3	88.3
Model B: NafeDrake	− 12.8	29.9	− 110.7	101.2
Model C: CM95	− 30.7	27.3	− 147.0	69.3
Model C: NafeDrake	− 15.2	27.0	− 118.6	105.7

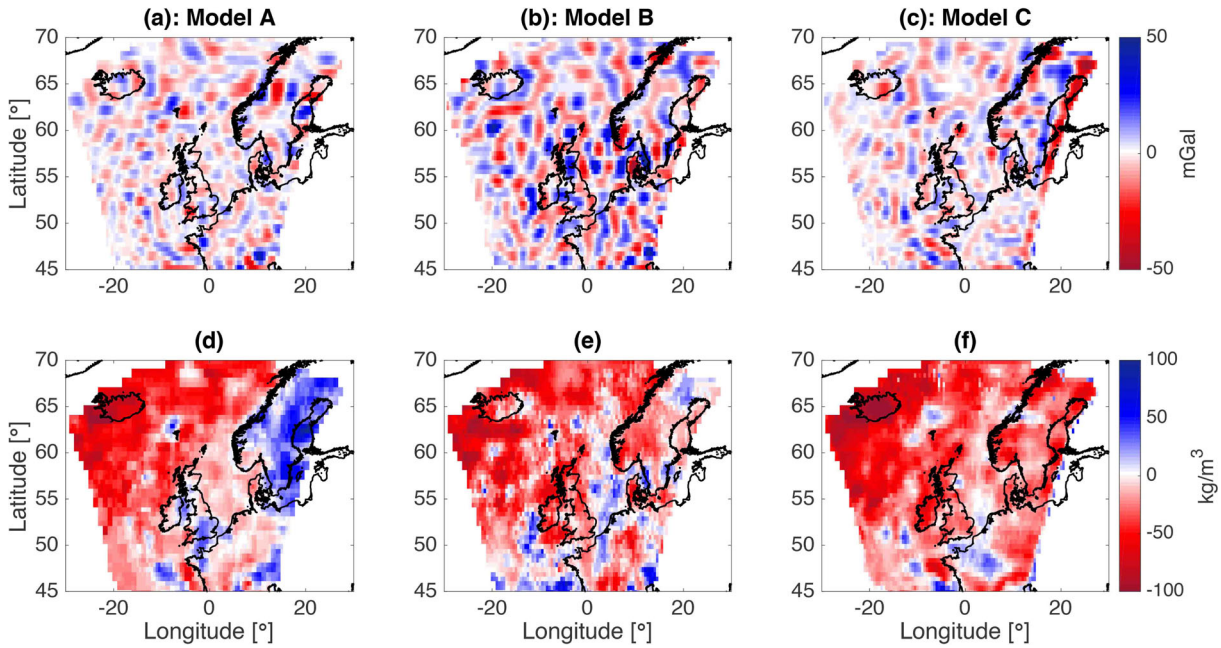

Figure 6. The top part of the figure shows the gravity field residuals of the different models: (a) EIGEN6C—Model A, (b) EIGEN6C—Model B and (c) EIGEN6C—Model C. The bottom part of the figure shows the corresponding lithospheric densities for three cases: (d) Model A using CRUST1.0 for the crustal model, (e) Model B using EuCrust-07 model for the crustal model and the Christensen and Mooney conversion relations, and (f) Model C using the regional model for the crustal model and the Gardener/Christensen and Mooney conversion relations.

pronounced density anomaly underneath Norway and Sweden, whereas Models B and C show more small-scale features in the area. Moreover, the value of the density anomalies are largest in Model A (-100 kg m^{-3}). Another distinct feature that is different between the three models is the density anomaly northwest of the Faroe Islands. This density anomaly could be attributed to the different Moho geometries in the crustal models. The density underneath the British Isles is similar for Models B and C, but differs from Model A. This could be attributed the improved V_P measurements available in that area for Models B and C.

Some geologically interesting locations are discussed in the following section (see Fig. 1 for location markers). One of the biggest lithospheric density mismatch is in the Fennoscandia region, where the density values between Models A and C differ more than 150 kg m^{-3}. We hypothesize that CRUST1.0 is underestimating the density in the cratonic area. This is corroborated by lithospheric modelling of the Fennoscandian craton (Kozlovskaya *et al.* 2004), where similar conclusions about the underestimated crustal density in CRUST1.0 have been made. Moreover, the lateral variations in the upper mantle underneath South Norway (Maupin *et al.* 2013) are visible in Models B and C, but do not show up in Model A. This distinct mantle anomaly was needed to explain the isostatic compensation of the mountain range in South Norway (Ebbing 2007; Maupin *et al.* 2013).

Furthermore, in the Porcupine sedimentary basin, offshore southwest Ireland, we can see more regional differences in the lithospheric density distribution. It is known that sedimentary basins are a large source of error in gravity modelling, because of uncertainty in their geometry and density distribution. The Mid-Norwegian Basin shows very local differences in lithospheric densities, but these density residuals can be considered small. In the Porcupine basin, Model C shows distinct features in the lithosphere that are related to the Porcupine sedimentary basin, whereas in Model A these are less prominent. To comply with isostasy in this area, the lithosphere needs to have a high density to compensate for the deep sedimentary basin. Local density differs in the lithosphere with approximately 75 kg m^{-3} between Models A and C. These differences are due to the extra information in Model C from new seismic profiling of the Porcupine basin. The density structure correlates well with the free-air anomaly of that region (Reston *et al.* 2001). Oddly, a distinct light density anomaly is situated underneath the positive anomaly. This particular signature can be explained because the sedimentary basin is divided by a volcanic ridge due to extensional stresses allowing basaltic rocks to rise into the upper part of the crust (Reston *et al.* 2001). Local depletion of the mantle could explain the strip of low lithospheric density surrounded by the high density needed to compensate the sedimentary basin.

In addition, Model B predicts high density features underneath the crust of the North Sea, that are not visible in Models A and C. These density features are not related to any geological structures, such as the North Sea Graben, and might be artefacts. Furthermore, in the proximity of the Faroe Islands the feature discussed earlier can also be seen in the lithosphere densities. All models have a high density just north of the Faroe islands. Model A shows a single density structure, whereas Models B and C show a double feature. This structure does not correlate to the bathymetry in the area, but does correlate with the Moho geometry. The deep Moho in the regional models need high density in the lithosphere for compensation. There is evidence for magmatic underplating in this region (Richardson *et al.* 1998), which greatly affects the radial density distribution. When this structure is not taken into account, for example because of low radial resolution of the crustal model, it introduces errors in the lithosphere model.

Continuing the comparison, a difference in lithospheric density can be seen onshore France. A positive density anomaly underneath the Paris Basin is visible in Models B and C. Model A does not show this feature. Again, the high density can be explained by isostasy to compensate the sedimentary basin, where relatively lighter

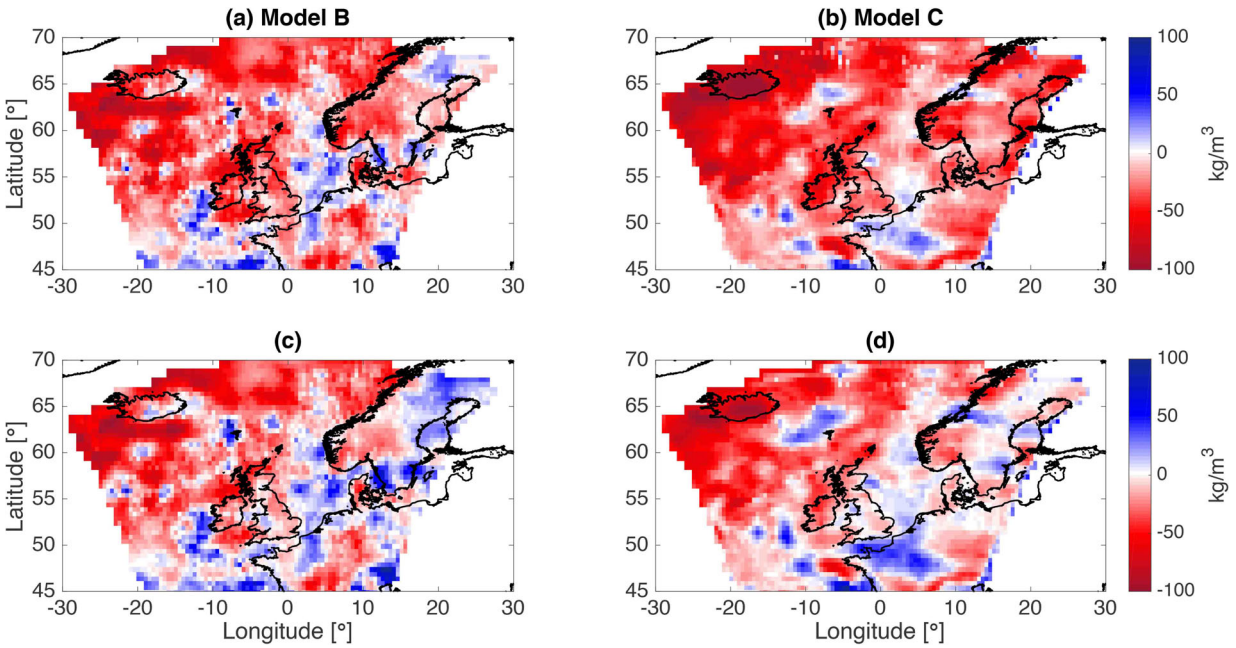

Figure 7. Lithosphere density maps of (a) Model B using the Christensen and Mooney conversion relations for the crustal structures, (b) Model C using the Christensen and Mooney conversion relations, (c) Model B using the Nafe–Drake conversion relations for the crustal structures, and (d) Model C using the Nafe–Drake conversion relations.

material is abundant. Overall, the regional model results show that the different crustal models do have an effect on the determination of lithospheric structures from gravity data. This comparison shows that local density features in the lithosphere can differ significantly due to the selected crustal model.

5.2 V_P-density conversion

To quantify the uncertainty introduced by the conversion of V_P to density both Models B and C are constructed using the two different conversion relations, discussed in Section 2.2. Fig. 7 shows the resulting lithospheric density maps. The spatial structure of the density maps is comparable for the different conversion relations. Some density anomalies are more pronounced using the Nafe–Drake conversion, like the Faroe anomaly in Model C. The mean and standard deviation of the differences between the two conversion relations for Model B are: $\mu_B = -7.7$ kg m^{-3} and $\sigma_B = 8.4$ kg m^{-3}. For Model C the values are similar of magnitude: $\mu_C = -15.5$ kg m^{-3} and $\sigma_C = 10.1$ kg m^{-3}. These variations are smaller than the variations due to different crustal models. This suggests that improvement in the seismic model of the crust is more important than the improvement of V_P to density conversion when considering the uncertainty of density in the lithosphere derived from gravity.

5.3 Long-wavelength signal removal

The bandwidth of the gravity observations should be selected such that it is sensitive to density anomalies of the lithosphere. Some studies state that spherical harmonic degree 10 is the appropriate lower truncation limit to remove deep mantle anomalies (Bowin 2000; Herceg *et al.* 2016), but others conclude that deep mantle dynamics have a significant contribution to higher wavelengths of the gravity field (Root *et al.* 2015). Deschamps *et al.* (2001) found that the geoid anomalies between spherical harmonic coefficients 11–16 are most sensitive to the lithosphere.

To study the effect of the truncation limit on the results, the limit of the gravity observations is varied during step 3. The upper truncation limit is fixed at degree and order 180, because there is only 1 × 1 arc-deg crustal information from CRUST1.0. We have varied the lower truncation limit to the following values: 3, 5, 10, 20, 30 and 35. We examine the overall density variation to see where the truncation has significant effect. Table 2 shows the statistics of the different lithospheric density solutions, their geoid, the amount of iterations needed, and the scaling factor used. Most of the variation (σ) in the density values is between 22 and 26 kg m^{-3} to adjust the isostatic model, such that it fits with the gravity field observations. Solutions with lower truncation degree limit (three to five) show a slightly smaller standard deviation than with a higher truncation degrees (10–35).

The spatial variation between solutions with different truncation are shown in Fig. 8. The density variation between the solutions with spherical harmonic truncation 3 and 35 is around ±20 kg m^{-3}. The largest variation is a west-east trend and is situated in the spherical harmonic coefficients 3 to 10, as can be seen in Fig. 8(b). Fig. 8(c) shows the variation between the solution using 10 and 35. Here, can be seen that the choice of truncation between 10 and 35 introduces an uncertainty of approximately ±5 kg m^{-3} in the computed density models. Overall, the statistical results of the lithosphere models with higher truncation limits do not differ significantly. From this evidence, we suggest using a truncation limit of degree 10 to remove deep mantle effects, which agrees with other studies.

5.4 Reference model

To study the effect of the chosen reference model in eq. (1) the model is varied to see the effects on the final result. The selected

Table 2. Statistical values of lithospheric density solutions and their fit to the observed geoid using different bandwidth selections in the iterative density fitting process. The models are depicted by their spherical harmonic truncation. μ and σ are mean and standard deviation, respectively.

Spectral bandwidth	Density μ (kg m^{-3})	σ (kg m^{-3})	min (kg m^{-3})	max (kg m^{-3})	Geoid fit 3σ (m)	# of iterations	Scaling factor
Isostatic	− 13.6	24.2	− 94.4	96.5			
3–180	− 9.3	22.6	− 94.4	100.8	2.7	25	0.15
5–180	− 15.1	22.6	− 98.6	93.4	3.0	20	0.1
10–180	− 15.2	25.3	− 111.5	99.9	1.6	14	0.5
20–180	− 14.5	26.0	− 112.4	100.6	1.2	8	1
30–180	− 14.6	26.5	− 116.4	102.7	0.9	8	1.5
35–180	− 14.3	26.2	− 113.4	101.7	1.1	5	2

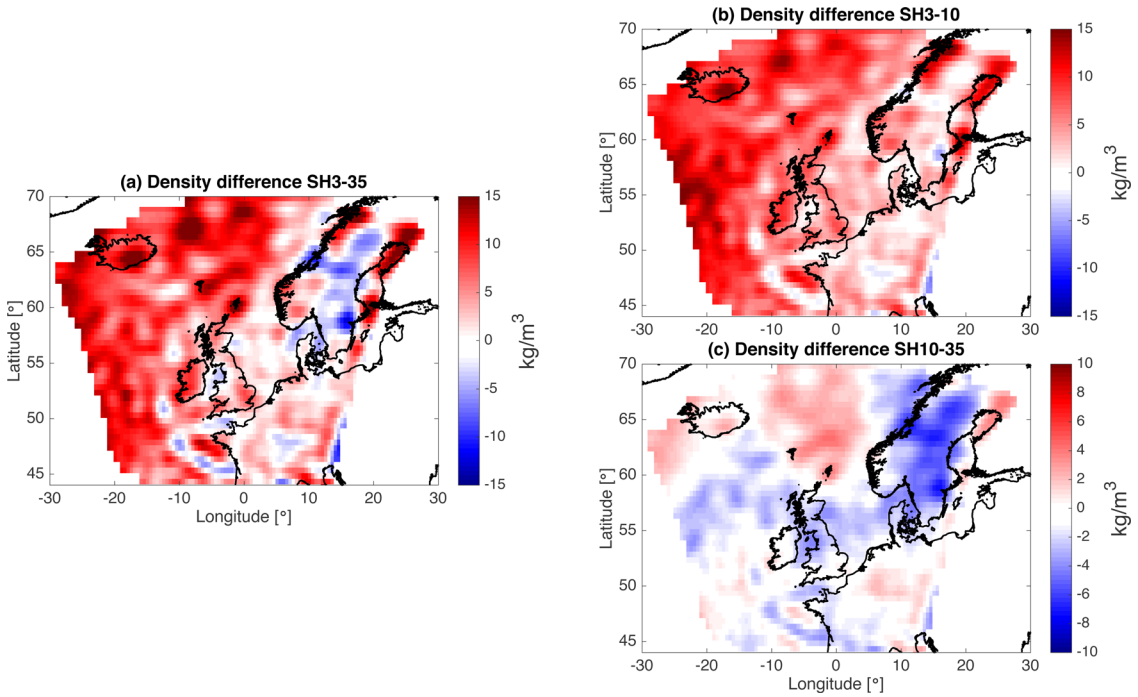

Figure 8. Density variation in the lithosphere when using different spherical harmonic truncations. (a) the difference in density between models using a lower truncation limit of 3 and 35. (b) the difference in density between models using a lower truncation limit of 3 and 10. (c) the difference in density between models using a lower truncation limit of 10 and 35.

reference model, or nominal model, used in this study has 30 km crustal thickness with crustal density of 2850 kg m^{-3}, complemented by the 270 km thick mantle layer with a density of 3300 kg m^{-3}. The reference model is varied by changing the mantle density between 3200 and 3400 kg m^{-3} with increments of 25 kg m^{-3}. The chosen variation in mantle densities encompasses enough uncertainty to quantify the effect of the reference model on the final result.

The resulting lithosphere density anomalies are inspected to assess the effects of the changes to the reference model. The results show that the lithosphere densities differ $\pm$20 kg m^{-3} from the densities in the nominal model in extreme cases of averaged mantle densities of 3200 and 3400 kg m^{-3}. The other models have smaller differences with the nominal reference model results (see Fig. 9). All density differences have a correlation with the Moho geometry of the chosen crustal model. This correlation can be explained because the model is trying to balance mantle and crustal masses, such that they fit the gravity field. When the reference mantle density is changed, the equilibrium is changed by an amount of mass that correlates to the Moho geometry.

5.5 Uncertainty in the LAB model

Finally, to examine the influence of uncertainties in the LAB model, Eq. (1) is evaluated for a model with a lithosphere thickness (D_{lith}) and a model with a lithosphere thickness plus an uncertainty ($D_{\text{lith}} + \Delta D$). By combining the two relations and neglecting the spherical representation, the following relation is obtained:

$$\Delta\rho_{\text{old}} D_{\text{lith}} = (\rho_{\text{lith}} - \rho_{\text{asth}})\Delta D + \Delta\rho_{\text{new}}(D_{\text{lith}} + \Delta D). \quad (5)$$

Typical errors in LAB depth underneath cratons are found to be around 10 per cent (Kuskov *et al.* 2014). An uncertainty of the LAB thickness of 10 per cent, $\frac{\Delta D}{D_{\text{lith}}} = 0.1$, is substituted to eq. (5). This results in a relationship for the density of the lithosphere

$$\Delta\rho_{\text{new}} = \frac{\Delta\rho_{\text{old}} - 0.1(\rho_{\text{lith}} - \rho_{\text{asth}})}{1.1}. \quad (6)$$

With this relation it can be proven that the density in the lithosphere also has around 10 per cent uncertainty, which is around $\pm$11 kg m^{-3} for the $\pm$110 kg m^{-3} variation in this study area.

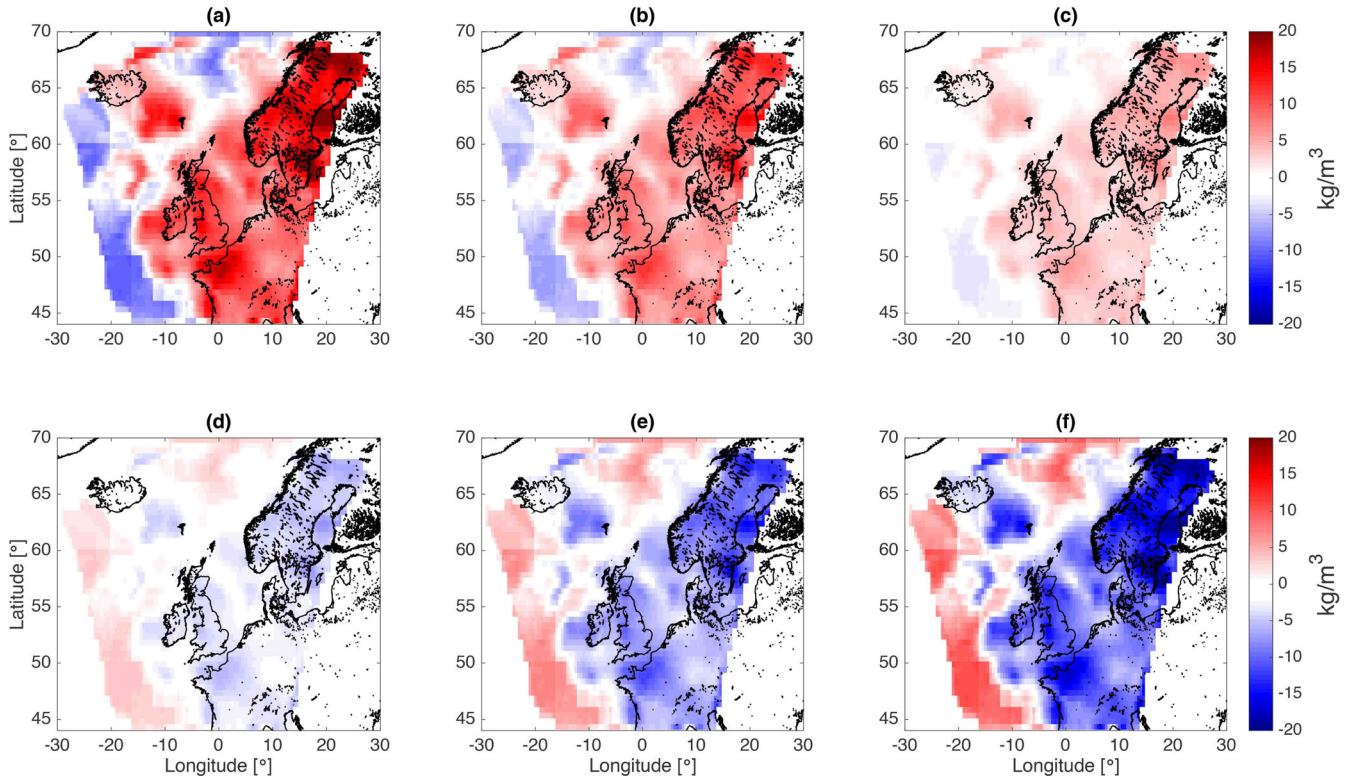

Figure 9. Density anomaly difference in the lithosphere when using different reference mantle density compared to the nominal model: (a) 3275 kg m^{-3}, (b) 3250 kg m^{-3}, (c) 3225 kg m^{-3}, (d) 3325 kg m^{-3}, (e) 3350 kg m^{-3}, (f) 3375 kg m^{-3}.

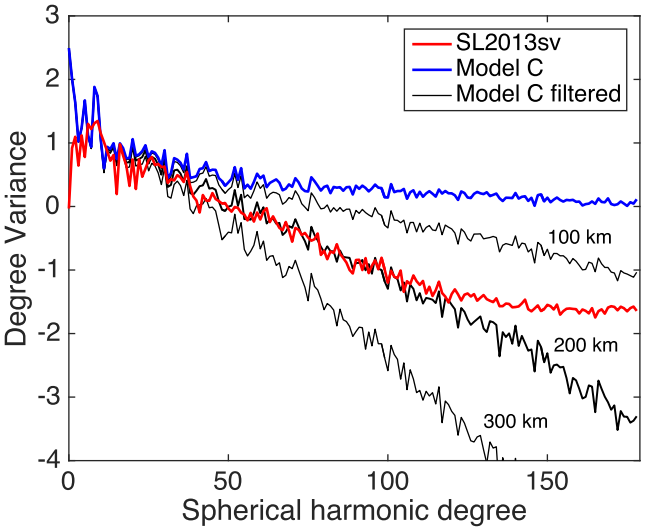

Figure 10. The spectral degree variance of the lithosphere density derived from V_S anomalies of SL2013sv model (red) and lithosphere density anomalies of Model C using the Nafe–Drake crustal conversion (blue). The black lines are the filtered densities of Model C using different Gaussian half-widths: 100, 200 and 300 km.

6 COMPARISON TO TOMOGRAPHY

The independently determined lithosphere structures from gravity modelling can be compared with models of lithospheric structures from seismic tomography. However, Fig. 10 shows the gravity-based models have a different spectral signature to the tomography model. Over the complete spectrum, the degree variance of the gravity-based models is much larger. In order to make the spectral signature comparable, we apply a Gaussian filter to the gravity-based density models such that short-wavelength features are reduced (Jekeli 1981), as SL2013sv is made with a nodal spacing of around 280 km (Schaeffer & Lebedev 2013). After studying several limits it was found that applying a Gaussian filter with a half-width of 200 km best approaches the spectral signature of the *S*-wave model. This can be seen in Fig. 10. Here, the gravity-based model that is filtered with a 200 km half-width Gaussian filter is almost completely overlapping with the degree variance of the V_S model. After this filter is applied, the spherical harmonic coefficients equal to and lower than degree and order 10 are truncated, because these were also truncated in the gravity fitting process. The filtered results are shown in Fig. 11.

After the filtering, the tomographic and the gravity-based models have a density variation and spatial structure of similar character. The main features of the lithosphere are represented by all four models. The density anomalies that mark the Icelandic region are represented by all models, as are the large scale anomalies around the British Isles. The *S*-wave based densities show a density anomaly underneath Scotland and Ireland, which is best represented by Model C. The southwest density high was not seen in the unfiltered gravity-based models, but is now present in all models. Underneath Denmark and Germany, the density low is also present in all models except Model B. This density signal could be a remnant of the North Sea anomalies. However, the density high underneath the west coast of France is best represented in Model C. Models A and B underestimate the inland extent of the anomaly, failing to model the Paris Basin signal. Moreover, there are other large-scale features in the seismic observations that cannot be reproduced by the gravity-based lithosphere models. Fennoscandia is different in all gravity-based models. Model A overestimates the density low due to the cratonic area, whereas Model C underestimates this feature.

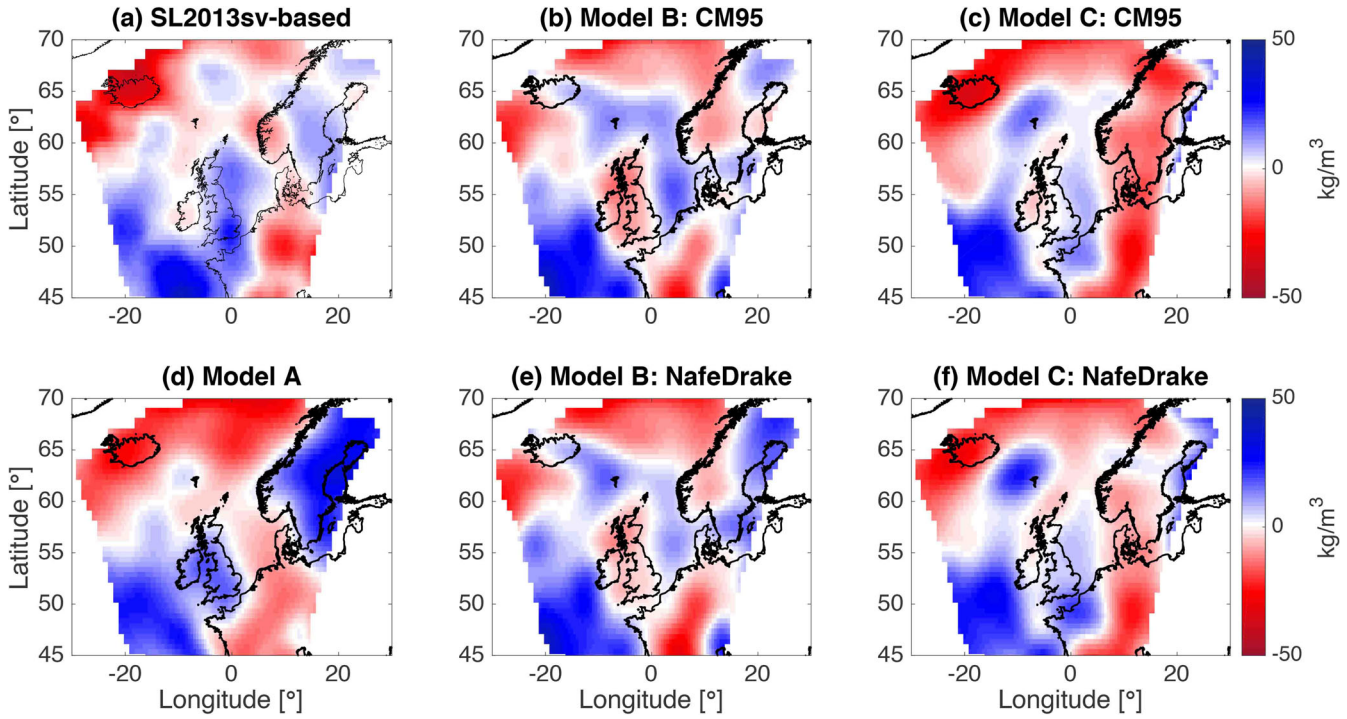

Figure 11. Lithospheric densities from the *S*-wave velocity conversions and gravity-based solutions for Models A–C. The gravity-based results are filtered using a Gaussian filter with 200 km half-width.

Table 3. Statistical values of the Gaussian filtered lithospheric density fields of the tomographic model (SL2013sv) and the gravity-based models. The differences between the tomographic model and the gravity-based models are in the bottom part of the table. μ and σ are mean and standard deviation, respectively.

	Density			
	μ	σ	min	max
Model	(kg m^{-3})	(kg m^{-3})	(kg m^{-3})	(kg m^{-3})
SL2013sv	0.52	12.9	− 39.5	39.4
Model A	0.37	15.1	− 32.6	34.5
Model B: CM95	1.38	11.5	− 27.9	40.7
Model B: NafeDrake	1.20	12.4	− 32.0	40.7
Model C: CM95	− 3.41	13.5	− 35.6	28.5
Model C: NafeDrake	− 0.57	12.7	− 30.9	28.8
SL2013sv - Model A	0.15	11.5	− 34.4	26.5
SL2013sv - Model B: CM95	− 0.86	11.9	− 42.1	28.1
SL2013sv - Model B: NafeDrake	− 0.68	12.1	− 43.0	27.0
SL2013sv - Model C: CM95	3.93	9.4	− 23.0	26.9
SL2013sv - Model C: NafeDrake	1.08	8.8	− 30.3	24.8

Moreover, north of the British Isles a large misfit is seen between the lithospheric density estimates. The Faroe anomaly, discussed in Section 5 and most pronounced in Models B and C, is not seen in the *S*-wave model. Model A shows a much less pronounced density anomaly in the Faroe Island area. On the contrary, a positive anomaly northeast of the Faroe Islands in the Norwegian Sea is seen in the *S*-wave model, but is not present in all the gravity-based models.

Table 3 shows the density comparison between the filtered models. Now, the density values of the tomographic model are similar to the gravity-based models with density variations of ±30–40 kg m^{-3}. These values are much lower than other gravity studies have reported (±70–150 kg m^{-3}) (Kaban *et al.* 2004; Herceg *et al.* 2016), as well as our results for the unfiltered models (±110 kg m^{-3}). This indicates that it is important that both modelling approaches have the same spectral content. However, we have seen that the main differences are due to local features. This is also corroborated by the bottom part of Table 3, where the differences between the tomographic and the gravity-based lithosphere models are presented. As in the unfiltered case, Model C (Nafe–Drake) performs best, but also here the differences between the other models are not significant. The main differences are due to the dissimilar modelling of Fennoscandia by Model A and large anomalies at the Faroe islands and the Porcupine basin in Models B and C.

With the filtered density values we can compute laterally varying conversion factors. Fig. 12 shows the estimated conversion factor between the *S*-wave velocities and gravity-based densities from Model C using the Nafe–Drake conversion. The colours depict the magnitude of the conversion factor. Blue depicts positive values and red for negative, whereas grey illustrates zones that are undetermined, because of our cut-off constraints discussed in Section 3.2. Some correlation between the conversion factor and tectonic regions can be deduced. A low conversion factor is seen in central Fennoscandia, which could mean that the compositional effect is more important than the thermal effect on the V_S to density conversion in that area. Cratonic areas are thought to have different composition due to depletion of the mantle material (Jordan 1979). Further to the south a negative conversion factor is present at the Tornquist zone (Bock *et al.* 2001). Here, the transition between cratonic and continental lithosphere is present. More positive conversion factors are seen in the continental region of western Europe, including the English part of the British Isles. Only western Ireland shows a small negative anomaly, becoming more positive towards the east, which could be related to the Proto-Ireland plume (Landes *et al.* 2007; Fullea *et al.* 2014; Jones *et al.* 2014). The plume had a thinning effect on the solid lithosphere and changed the composition of the lithosphere (Al-Kindi *et al.* 2003; Landes *et al.* 2007). Comparing our results with the density models of Fullea *et al.* (2014),

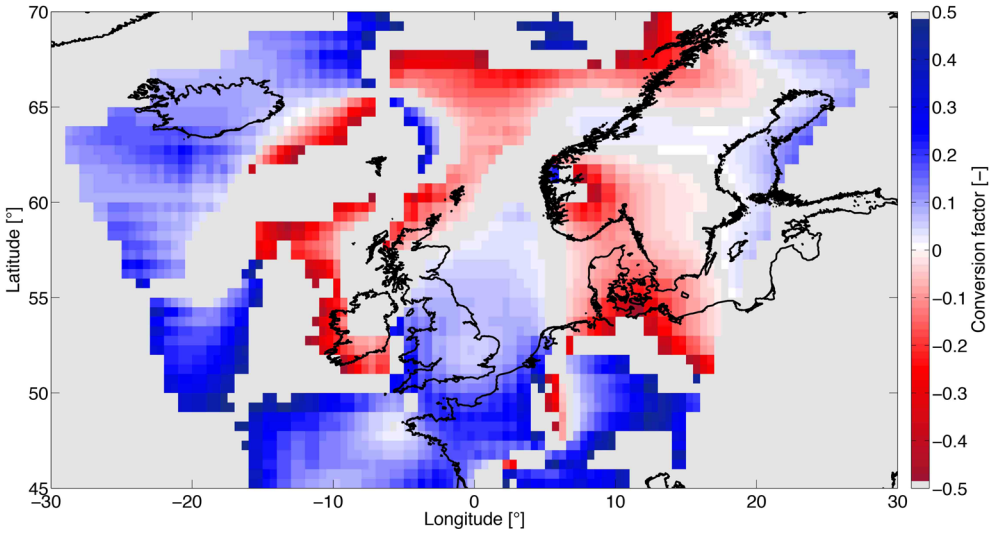

Figure 12. The laterally varying conversion factor between the *S*-wave velocities of SL2013sv in the lithosphere and the gravity-based densities of Model C (Nafe–Drake). The gravity-based results are filtered with a Gaussian filter (half-width of 200 km). The grey zones are areas where the conversion factor could not be determined.

the changing conversion factor could be explained by the proposed compositional change between western and eastern Ireland. Furthermore, a clear change in conversion factor cuts through southern Scotland and central Ireland, depicting the old boundary between Avalonia and Laurentia. North of this boundary, the conversion factor is negative. It separates thinned cratonic crust of Laurentia to the northwest from Proterozoic basement of Gondwanan age (Avalonia) to the southeast. Here, both thermal and compositional processes would dominate the density of the lithosphere. Overall, this shows that the determination of density from seismic and from gravity data can help distinguish tectonic settings.

7 CONCLUDING REMARKS

In this study, we have compared lithospheric structures determined by gravity-based and seismic-based modelling. The drawbacks of seismic modelling are uneven distribution of observation data, the dependency on an *a priori* crustal model, coupled uncertainties between velocity and depth-to-interface, and the uncertain relations between wave velocity and physical parameters, such as density, temperature, and composition. The uncertainty in gravity-based modelling is based on the introduction of constraints to eliminate deep mantle effects and the crustal gravity signal. Furthermore, we have proposed a novel gravity modelling methodology to estimated lithospheric density anomalies, using a crustal model, lithospheric isostasy, and gravity field observations.

The three different crustal models used for eliminating the crustal gravity signal are: CRUST1.0, EuCrust-07, and a regional *P*-wave velocity model. The variation in crustal *P*-wave velocity to density conversion show less differences between the conversion methodologies than differences due to different crustal models. The uncertainty in the crustal models is mainly caused by data acquisition. The regional crustal model in this study shows a small improvement in misfit to the observed gravity field, but the averaged differences between the three models are not significant. The different crustal models can cause variations in lithosphere density up to ± 110 kg m^{-3}. The different conversion relations introduce an uncertainty in the lithospheric density of ± 10 kg m^{-3}. Moreover, the effect of different truncations of the spherical harmonic representation of the gravity field does not have a significant effect (± 5 kg m^{-3}), when a lower truncation value of 10–35 is chosen. Also, the reference model used in the isostatic step of the methodology does not have a significant effect. The estimated lithosphere density varied by not more than ± 20 kg m^{-3} due to reference model changes. Finally, the LAB uncertainty causes density variations in the lithosphere of around 10 per cent.

The variation in density needed to fit the gravity field in the lithosphere (± 110 kg m^{-3}) is larger than the density variations obtained by converting the *S*-wave velocity observations (± 35 kg m^{-3}), due to spectral imbalance. After filtering the gravity-based lithosphere solutions, we have shown that tomographic and gravity-based lithosphere models are comparable. The best Gaussian filter to compare our gravity-based results to density estimated from the tomography model SL2013sv has a half-width of 200 km.

With the proposed gravity-based lithosphere modelling, density structures can be determined independently from mantle tomography. However, high-resolution V_P crust models are needed to reduce the uncertainty in the estimated density maps. The independent density estimates can be used together with tomographic models to compute lateral variations in the conversion factor, giving insights on the importance of compositional and thermal effects on seismic velocity anomalies.

ACKNOWLEDGEMENTS

We would like to thank Wolfgang Swillius for helpful discussions on the topic. Also, we are grateful to Magdala Tesauro for her help with using the EUCrust-07 model and Mikhail Kaban for supplying the corresponding sediment density model. Finally, we like to thank the editor Kosuko Heki for his help in the review process and Juan Carlos Afonso and an anonymous reviewer for their thorough review of the manuscript. This study was funded by NWO under the project ALW-GO-AO/10-10.

REFERENCES

Afonso, J.C., Fernàndez, M., Ranalli, G., Griffin, W.L. & Connolly, J.A.D., 2008. Integrated geophysical-petrological modeling of the lithosphere and

sublithospheric upper mantle: methodology and applications, *Geochem. Geophys. Geosyst.,* **9**(5), 1–36.

Afonso, J.C., Fullea, J., Griffin, W.L., Yang, Y., Jones, A.G., Connolly, J.A.D. & O'Reilly, S.Y., 2013a. 3-D multiobservable probabilistic inversion for the compositional and thermal structure of the lithosphere and upper mantle. I: a priori petrological information and geophysical observables, *J. geophys. Res.,* **118,** 2586–2617.

Afonso, J.C., Fullea, J., Yang, Y., Connolly, J.A.D. & Jones, A.G., 2013b. 3-D multi-observable probabilistic inversion for the compositional and thermal structure of the lithosphere and upper mantle. II: General methodology and resolution analysis, *J. geophys. Res.,* **118,** 1650–1676.

Afonso, J.C., Moorkamp, M. & Fullea, J., 2016a. Imaging the lithosphere and upper mantle: where we are at and where we are going, in *Integrated Imaging of the Earth: Theory and Applications,* Geophysical Monograph 218, 1st edn, Moorkamp, M., Lelièvre, P. G., Linde, N. & Khan, A., John Wiley & Sons, Inc.

Afonso, J.C., Rawlinson, N., Yang, Y., Schutt, D.L., Jones, A.G., Fullea, J. & Griffin, W.L., 2016b. 3-D multiobservable probabilistic inversion for the compositional and thermal structure of the lithosphere and upper mantle: III. Thermochemical tomography in the Western-Central U.S., *J. geophys. Res.,* **121,** 1–34.

Al-Kindi, S., White, N., Sinha, M., England, R. & Tiley, R., 2003. Crustal trace of a hot convective sheet, *Geology,* **31**(3), 207–210.

Amante, C. & Eakins, B.W., 2009. ETOPO1 1 Arc-Minute Global Relief Model: Procedures, Data Sources and Analysis. NOAA Technical Memorandum NESDIS NGDC-24. National Geophysical Data Center, NOAA.

Artemieva, I., 2001. *The Lithosphere: An Interdisciplinary Approach,* 421 pp., Cambridge Univ. Press.

Artemieva, I. & Thybo, H., 2013. EUNAseis: A seismic model for Moho and crustal structure of Europe, Greenland, and the North Atlantic region, *Tectonophysics,* **609,** 97–153.

Brocher, T.M., 2005. Empirical relations between elastic wavespeeds and density in the Earth's crust, *Bull. seism. Soc. Am.,* **95** (6), 2081–2092.

Bock, G. *et al.*, 2001. Seismic probing of Fennoscandian lithosphere, *EOS, Trans. Am. geophys. Un.,* **82**(50), 621–636.

Bowin, C., 1991. The Earth's gravity field and plate tectonics, *Tectonophysics,* **187,** 69–89.

Bowin, C., 2000. Mass Anomalies and the Structure of the Earth, *Phys. Chem. Earth,* **25**(4), 343–353.

Cammarano, F., Goes, S., Vacher, P. & Giardini, D., 2003. Inferring upper mantle temperatures from seismic velocities, *Phys. Earth planet. Inter.,* **139,** 197–222.

Cammarano, F., Tackley, P. & Boschi, L., 2011. Seismic, petrological and geodynamical constraints on thermal and compositional structure of the upper mantle: global thermochemical models, *Geophys. J. Int.,* **187,** 1301–1318.

Christensen, N.I. & Mooney, W.D., 1995. Seismic velocity structure and composition of the continental crust: a global view, *J. geophys. Res.,* **100,** 9761–9788.

Debayle, E. & Ricard, Y., 2012. A global shear velocity model of the upper mantle from fundamental and higher Rayleigh mode measurements, *J. geophys. Res.,* **117,** B10308, doi:10.1029/2012JB009288.

DeGiorgio, R., 2012. A new 3D velocity model of Scandinavia from seismic data, *Master's thesis,* University of Leicester.

Deschamps, F., Snieder, R. & Trampert, J., 2001. The relative density-to-shear velocity scaling in the uppermost mantle, *Phys. Earth planet. Inter.,* **124,** 193–211.

Ebbing, J., 2007. Isostatic density modeling explains the missing root of the Scandes, *Norwegian J. Geol.,* **87,** 13–20.

Forte, A.M., 2007. Constraints on seismic models from other disciplines—implications for mantle dynamics and composition, in *Treatise of Geophysics,* Vol. 1, pp. 805–857, Elsevier.

Forte, A.M. & Mitrovica, J.X., 2001. Deep-mantle high-viscosity flow and thermochemical structure inferred from seismic and geodynamic data, *Nature,* **410,** 1049–1056.

Forte, A.M., Peltier, W.R., Dziewonski, A.M. & Woodward, R.L., 1993. Dynamic surface topography: a new interpretation based upon mantle flow models derived from seismic tomography, *Geophys. Res. Lett.,* **20**(3), 226–228.

Forte, A.M., Woodward, R.L. & Dziewonski, A.M., 1994. Joint inversion of seismic and geodynamic data for models of three-dimensional mantle heterogeneity, *J. geophys. Res.,* **99**(B11), 21 857–21 877.

Foulger, G.R. *et al.*, 2013. Caveats on tomographic images, *Terra Nova,* **25,** 259–281.

Fullea, J., Muller, M.R., Jones, A.G. & Afonso, J.C., 2014. The lithosphere-asthenosphere system beneath Ireland from integrated geophysical-petrological modeling. II: 3D thermal and compositional structure, *Lithos,* **189,** 49–64.

Gardner, G.H.F., Gardner, L.W. & Gregory, A.R., 1974. Formation velocity and density—the diagnostic basics for stratigraphic traps, *Geophysics,* **39**(6), 770–780.

Griffin, W.L., O'Reilly, S.Y., Afonso, J.C. & Begg, G.C., 2009. The composition and evolution of lithospheric mantle: a re-evaluation an its tectonic implications, *J. Petrol.,* **50**(7), 1185–1204.

Hamza, V.M. & Vieira, F.P., 2012. Global distribution of the lithosphere-asthenosphere boundary: a new look, *Solid Earth,* **3,** 199–212.

Herceg, M., Artemieva, I.M. & Thybo, H., 2016. Sensitivity analysis of crustal correction for calculation of lithospheric mantle density from gravity data, *Geophys. J. Int.,* **204,** 687–696.

Jekeli, C., 1981. Alternative methods to smooth the Earth's gravity field, Technical Report No. 327, Department of Geodetic Science and Surveying, The Ohio State University, Columbus, OH.

Jones, A.G., Afonso, J.C., Fullea, J. & Salajegheh, F., 2014. The llithosphere-asthenosphere system beneath Ireland from integrated geophysical-petrological modeling—I: Observations, 1D and 2D hypothesis testing and modeling, *Lithos,* **189,** 28–48.

Jordan, T.H., 1975. Composition and development of the continental tectosphere, *Nature,* **274,** 544–548.

Jordan, T.H., 1978. Lateral heterogeneity and mantle dynamics, *Nature,* **257,** 745–750.

Jordan, T.H., 1979. The Deep Structure of the Continents, *Sci. Am.,* **240**(1), 92–107.

Kaban, M.K., Schwintzer, P. & Reigber, Ch., 2004. A new isostatic model of the lithosphere and gravity field, *J. Geod.,* **78,** 368–385.

Kaban, M.K., Tesauro, M., mooney, W.D. & Cloetingh, S., 2014. Density, temperature, and composition of the North American lithosphere—new insights from a joint analysis of seismic gravity, and mineral physics data: 1. Density structure of the crust and upper mantle, *Geochem. Geophys. Geosyst.,* **15,** 4781–4807.

Kaban, M.K., Stolk, W., Tesauro, M., El Khrepy, S., Al-Arifi, N., Beekman, F. & Cloetingh, S.A.P.L., 2016. 3D density model of the upper mantle of Asia based on inversion of gravity and seismic tomography data, *Geochem. Geophys. Geosyst.,* **17,** 1–21.

Karato, S., 2008. *Deformation of Earth Materials: An Introduction to the Rheology of Solid Earth,* Cambridge Univ. Press, p. 377.

Kelly, A., England, R.W. & Maguire, P.K.H., 2007. A crustal seismic velocity model for the UK, Ireland and surrounding seas, *Geophys. J. Int.,* **171,** 1172–1184.

Khan, A., Koch, S., Shankland, T.J., Zunino, A. & Connolly, J.A.D., 2015. Relationships between seismic wave-speed, density, and electrical conductivity beneath Australia from seismology, mineralogy, and laboratory-based conductivity profiles, in *The Earth's Heterogeneous Mantle,* Chapter 5, eds Khan, A. & Deschamps, F., Springer International Publishing.

Kinck, J.J., Husebye, E.S. & Larsson, F.R., 1993. The Moho depth distribution in Fennoscandia and the regional tectonic evolution from Archean to Permian times, *Precambrian Res.,* **64,** 23–51.

Korsman, K., Korja, T., Pajunen, M., Virransalo, P. & GGT/SVEKA Working Group, 1999. The GGT/SVEKA Transect: structure and evolution of the continental crust in the Paleoproterozoic Svecofennian Orogen in Finland, *Int. Geol. Rev.,* **41,** 287–333.

Kozlovskaya, E., Janik, T., Yliniemi, J., Karatayev, G. & Grad, M., 2004. Density-velocity relationship in the upper lithosphere obtained from P- and S-wave velocity models along the EUROBRIDGEÕ97 seismic profile and gravity data, *Acta Geophys. Pol.,* **52**(4), 397–424.

Kuskov, O.L., Kronrod, V.A., Prokofyev, A.A. & Pavlenkova, N.I., 2014. Thermo-chemical structure of the lithospheric mantle underneath the Siberian craton inferred from long-range seismic profiles, *Tectonophysics,* **615–616,** 154–166.

Landes, M., Ritter, J.R.R. & Readman, P.W., 2007. Proto-Iceland plume caused thinning of Irish lithosphere, *Earth planet. Sci. Lett.,* **255,** 32–40.

Laske, G., Masters, G., Ma, Z. & Pasyanos, M., 2013. Update on CRUST1.0 - A 1-degree global model of Earth's crust, *Geophys. Res. Abstr.,* **15,** EGU2013-2658, http://igppweb.ucsd.edu/gabi/rem.html

Lekić, V. & Romanowicz, B., 2011. Inferring upper-mantle structure by full waveform tomography with the spectral element method, *Geophys. J. Int.,* **185,** 799–831.

Ludwig, W.J., Nafe, J.E. & Drake, C.L., 1970. Seismic refraction, in *The Sea,* Vol. 4, pp. 53–84, ed. Maxwell, A.E., Wiley-Interscience.

Maguire, P., England, R. & Hardwick, A., 2011. LISPB DELTA, a lithospheric seismic profile in Britain: analysis and interpretation of the Wales and southern England section, *J. Geol. Soc.,* **168,** 61–82.

Maupin, V. *et al.*, 2013. The deep structure of the Scandes and its relation to tectonic history and present-day topography, *Tectonophysics,* **602,** 15–37.

Novák, P. & Grafarend, E., 2006. The effect of topographical and atmospheric masses on space borne gravimetric and gradiometric data, *Stud. Geophys. Geod.,* **50,** 549–582.

Reston, T.J., Pennell, J., Stubenrauch, A., Walker, I. & Perez-Gussinye, M., 2001. Detachment faulting, mantle serpentinization, and serpentinite-mud volcanism beneath the Porcupine Basin, Southwest of Ireland, *Geology,* **29**(7), 587–590.

Richardson, K.R., Smallwood, J.R., White, R.S., Snyder, D.B. & Maguire, P.K.H., 1998. Crustal structure beneath the Faroe Islands and the Faroe-Iceland Ridge, *Tectonophysics,* **300,** 159–180.

Ritsema, J., Deuss, A., van Heijst, H.J. & Woodhouse, J.H., 2011. S40RTS: a degree-40 shear-velocity model for the mantle from new Rayleigh wave dispersion, teleseismic traveltime and normal-mode splitting function measurements, *Geophys. J. Int.,* **184,** 1223–1236.

Root, B.C., Novák, P., Ebbing, J., van der Wal, W. & Vermeersen, L.L.A., 2015. Glacial Isostatic Adjustment in the static gravity field of Fennoscandia, *J. geophys. Res.,* **120,** 503–518.

Root, B.C., Novák, P., Dirkx, D., Kaban, M.K., van der Wal, W. & Vermeersen, L.L.A., 2016. On a spectral method for forward gravity field modelling, *J. Geodyn.,* **97,** 22–30.

Rummel, R., Rapp, R.H., Sunkel, H. & Tscherning, C.C., 1988. Comparison of global topographic/isostatic models to the Earth's observed gravity field, Technical Report No. 388, Department of Geodetic Science and Surveying, The Ohio State University, Columbus, OH.

Schaeffer, A.J. & Lebedev, S., 2013. Global shear speed structure of the upper mantle and transition zone, *Geophys. J. Int.,* **194**(1), 417–449.

Schivardi, R. & Morelli, A., 2011. EPmantle: a 3-D transversely isotropic model of the upper mantle under the European Plate, *Geophys. J. Int.,* **185,** 469–484.

Shako, R. *et al.*, 2014. EIGEN-6C.A high-resolution global gravity combination model including GOCE data, in *Observation of the System Earth from Space - CHAMP, GRACE, GOCE and Future Missions,* pp. 155–161, eds Flechtner, F., Sneeuw, N. & Schuh, W.-D., Springer-Verlag.

Simmons, N.A., Forte, A.M., Boschi, L. & Grand, S.P., 2010. GyPSuM: a joint tomographic model of mantle density and seismic wave speeds, *J. geophys. Res.,* **115,** B12310, doi:10.1029/2010JB007631.

Sneeuw, N., 1994. Global spherical harmonic analysis by least-squares and numerical quadrature methods in historical perspective, *Geophys. J. Int.,* **118,** 707–716.

Steffen, H. & Wu, P., 2011. Glacial isostatic adjustment in Fennoscandia - A review of data and modeling, *J. Geodyn.,* **52,** 169–204.

Steinberger, B., 2016. Topography caused by mantle density variations: observations-based estimates and models derived from tomography and lithosphere thickness, *Geophys. J. Int.,* **205,** 604–621.

Stratford, W., Thybo, H., Faleide, J.I., Olesen, O. & Tryggvason, A., 2009. New Moho map for onshore southern Norway, *Geophys. J. Int.,* **178**(3), 1755–1765.

Tesauro, M., 2008. An integrated study of the structure and thermomechanical properties of the European lithosphere, *PhD thesis,* Amsterdam, The Netherlands: Faculty of Earth and Life Sciences, Vrije Universiteit.

Tesauro, M., Kaban, M.K., Mooney, W.D. & Cloetingh, S., 2014. NACr14: a 3D model for the crustal structure of the North American Continent, *Tectonophysics,* **631,** 65–86.

Turcotte, D.L. & Schubert, G., 2014. *Geodynamics,* Cambridge Univ. Press.

Panasyuk, S.V. & Hager, B.H., 2000. Models of isostatic and dynamic topography, geoid anomalies, and their uncertainties, *J. geophys. Res.,* **105**(B12), 28 199–28 209.

Vieira, F.P. & Hamza, V.M., 2010. Global heat loss: new estimates using digital geophysical maps and GIS techniques, in *Proceedings of the IV Symposium of the Brazilian Geophysical Society,* 14–17 November, pp. 1–6.

Zoback, M.L. & Mooney, W.D., 2003. Lithospheric buoyancy and continental intraplate stresses, *Int. Geol. Rev.,* **45,** 95–118.